nature sustainability

Article

https://doi.org/10.1038/s41893-025-01530-y

Photoelectrochemical production of disinfectants from seawater

Received: 4 September 2024

Accepted: 21 February 2025

Rui-Ting Gao[1,6], Zehua Gao[1,6], Nhat Truong Nguyen[2], Junxiang Chen[3], Xianhu Liu[4], Lei Wang[1] & Limin Wu[1,5]

Active chlorine, including HClO and ClO^-, is one of the most extensively used disinfectants. However, it is mainly produced through energy-consuming three-step chlor-alkali electrolysis of saturated brine using Cl_2 gases as intermediates. Here we report a photoelectrochemical synthetic pathway from natural seawater using a chloride-mediated $NbClO_x/BiVO_4$ photoanode. The photoanode presents an onset potential of 0.6 V versus a reversible hydrogen electrode (V_{RHE}) and over 500 h of stability in seawater under one sun illumination. The faradaic efficiency and selectivity of hypochlorite are close to 100% at 1.2–1.8 V_{RHE} with a yield of 119.9 ± 9 μmol cm^{-2} h^{-1} at 1.72 V_{RHE}. Meanwhile, value-added products of $Mg(OH)_2$ and $CaCO_3$ are obtained on the cathode, accompanied by hydrogen production. Further analyses show that the present process reduces electricity consumption by 77.16% and CO_2 emissions by 75.31%. Our findings suggest a strategy with combined safety, efficiency and economic feasibility for direct synthesis of active chlorine from seawater.

Active chlorine (AC) (including HClO and ClO^-) is a widely used disinfectant with important roles in biological, medical, environmental and chemical engineering applications (Fig. 1a)[1–4]. It is usually synthesized through a chlor-alkali process in industry[5,6]. However, this process involves the electrolysis of saturated brine (5–6 M) in highly purified water and thus produces substantial quantities of corrosive and toxic chlorine gas (Cl_2) in an acidic electrolyte ($pH < 3$) through a three-step reaction mechanism: the Vlomer step ($Cl^-(aq) \rightarrow Cl^* + e^-$), the Heyrovsky step ($Cl^* + Cl^-(aq) \rightarrow Cl_2 + e^-$) and the disproportionation of Cl_2 with water or alkali ($Cl_2 + H_2O \leftrightarrow HClO + HCl; Cl_2 + 2OH^- \leftrightarrow ClO^- + Cl^- + H_2O$)[7–9]. It is therefore highly desirable to develop alternatives to the current chlor-alkali process that can avoid Cl_2 production and efficiently convert Cl^- to ClO^- (Fig. 1b).

The chlor-alkali process is usually implemented in fresh or highly purified water, which accounts for less than 0.5% of directly available water resources[4]. The preparation process of highly purified water results in high energy consumption and high complexity in instrumentation. Alternatively, seawater, one of the most abundant natural resources, can be potentially used as an electrolyte to synthesize AC. However, seawater has a low Cl^- ion concentration, which increases the competition between the chlorine oxidation reaction (ClOR) and the oxygen evolution reaction (OER) during the chlor-alkali process, hindering the selective synthesis of AC[10–14]. In addition, the electrodes are usually composed of Ti plates loaded with precious metal oxides, which are seriously corroded by Cl^- ions, leading to their dissolution and deactivation during long-term operation[15,16]. Moreover, the complicated alkaline metal cations (for example, K^+, Na^+, Ca^{2+} and Mg^{2+}) from natural seawater usually even cover the anodes during the oxidation reaction, decreasing the stability of the electrodes[17].

---

[1]College of Chemistry and Chemical Engineering, College of Energy Material and Chemistry, Inner Mongolia Key Laboratory of Low Carbon Catalysis, Inner Mongolia University, Hohhot, China. [2]Department of Chemical and Materials Engineering, Gina Cody School of Engineering and Computer Science, Concordia University, Montreal, Quebec, Canada. [3]State Key Laboratory of Structural Chemistry, and Fujian Provincial Key Laboratory of Materials and Techniques toward Hydrogen Energy, Fujian Institute of Research on the Structure of Matter, Chinese Academy of Sciences, Fuzhou, China. [4]National Engineering Research Center for Advanced Polymer Processing Technology, Zhengzhou University, Zhengzhou, China. [5]Department of Materials Science and State Key Laboratory of Molecular Engineering of Polymers, Fudan University, Shanghai, China. [6]These authors contributed equally: Rui-Ting Gao, Zehua Gao. e-mail: wanglei@imu.edu.cn; wlm@imu.edu.cn

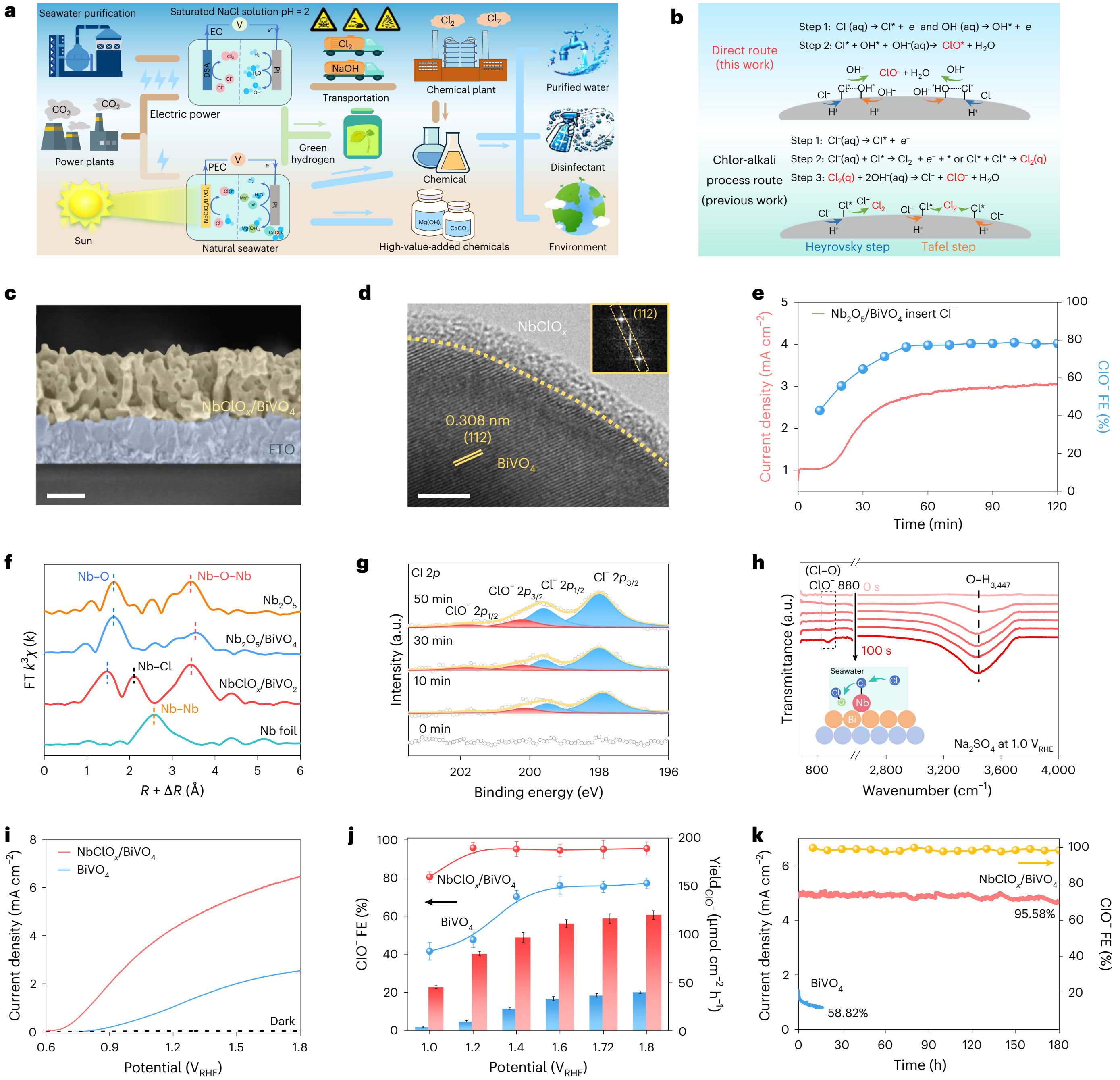

Fig. 1 | PEC disinfectant synthesis in natural seawater. a, PEC synthesis of disinfectants and related applications. EC, electrochemistry. **b**, Comparison of the classic chlor-alkali process and direct PEC disinfectant synthesis. Red part represents the generation process of Cl intermediates and products. **c**,**d**, Scanning electron microscopy (**c**) and high-resolution transmission electron microscopy (**d**) images of $NbClO_x/BiVO_4$. Scale bars, 500 nm (**c**) and 5 nm (**d**). FTO, fluorine-doped tin oxide. **e**, J–t curves and FE of $Nb_2O_5/BiVO_4$ polarized potentiostatically at 1.0 V_{RHE} in 0.5 M NaCl under AM 1.5 G illumination. **f**, The Nb K-edge Fourier-transformed EXAFS spectra (R-space) of $Nb_2O_5/BiVO_4$ and $NbClO_x/BiVO_4$ as well as Nb foil and Nb_2O_5 references. **g**, Cl 2p XPS spectra of $NbClO_x/BiVO_4$. **h**, In situ Fourier transform infrared spectroscopy with the OTTO configuration of $NbClO_x/BiVO_4$ in Na_2SO_4 at 1.0 V_{RHE}. **i**, Linear sweep voltammetry curves of $NbClO_x/BiVO_4$ and $BiVO_4$. **j**, FEs and yields of ClO^- at various voltages. The bars/balls represent the mean value for $n = 3$ experiments and data distribution is represented by the dots. **k**, Long-term stability and FEs of ClO^- of $NbClO_x/BiVO_4$ in natural seawater at 1.3 V_{RHE} in an H-cell.

Different from the traditional chlor-alkali process performed under a strong acidic environment, the thermodynamic theoretical equilibrium potential required for the electrochemical synthesis of AC increases with higher pH (Supplementary Fig. 1 and Supplementary Note 1), especially in neutral or alkaline electrolytes where the equilibrium potential exceeds 1.72 V versus a reversible hydrogen electrode (V_{RHE})[18]. Alternatively, photoelectrochemistry (PEC) provides a promising approach to synthesizing AC chemicals as it uses sustainable resources (that is, solar energy and seawater), which will substantially reduce CO_2 emissions and environmental pollution caused by electricity generation (Supplementary Fig. 2 and Supplementary Note 2)[19]. Bismuth vanadate ($BiVO_4$), which is easy to prepare, has a low cost and can absorb most of the visible light due to its suitable band edge position, has been recently investigated in several PEC applications, such as solar water splitting, fuel cells, glycerol oxidation and hydrogen peroxide synthesis[20–22]. It is therefore considered an appealing photoanode material for AC production. However, $BiVO_4$ suffers from inertness towards the selective adsorption and oxidation of Cl^- from natural seawater[23–25].

Here we address the above issues by proposing a unique chloride-mediated $NbClO_x/BiVO_4$ photoanode. This photoanode can be used for the direct synthesis of disinfectants from seawater through a two-step reaction mechanism, in which the AC on the photoanode can be synthesized by Cl* and OH* from seawater to substitute for the widely used three-step chlor-alkali strategy, aiming to avoid using massive amounts of Cl_2 as intermediates. The photoanode delivers a photocurrent density as high as 6.26 mA cm^{-2} at a voltage of 1.72 V_{RHE} with a low onset potential of 0.6 V_{RHE} under one sun illumination. The faradaic efficiency (FE) and selectivity of ClO^- are close to 100% at 1.2–1.8 V_{RHE}. This remarkable performance is maintained at 1.3 V_{RHE} over 500 h in seawater. The electricity consumption and CO_2 emissions of $NbClO_x/BiVO_4$ are 77.16% and 75.31% lower, respectively, than those of the commercial anode in the classical two-electrode system with the same amount of ClO^-. Furthermore, value-added products such as $Mg(OH)_2$, $CaCO_3$ and hydrogen can be obtained simultaneously on the cathode and serve to soften seawater. Our PEC device can convert 100 ml of seawater into 550 ppm of disinfectant in 22 h with a 1 cm^2 photoanode. This sustainable disinfectant synthesis method could find applications in various fields.

Results

Photoelectrochemical synthetic disinfectants

The as-prepared $BiVO_4$ sample following a reported method[26–28] was electrodeposited in a niobium oxalate precursor, followed by a thermal treatment for fabrication of $Nb_2O_5/BiVO_4$. $Nb_2O_5/BiVO_4$ was potentiostatically polarized in a NaCl electrolyte to form a Cl^--inserted sample ($NbClO_x/BiVO_4$) (Fig. 1c,d; the details are provided in Supplementary Figs. 3–7 and Supplementary Notes 3 and 4). According to the *J*–*t* plot in Fig. 1e, the photocurrent density of $Nb_2O_5/BiVO_4$ in 0.5 M NaCl increases from 0.78 to 3.04 mA cm^{-2} with time, and its FE substantially increases from 42.76% to 78.23% (Supplementary Fig. 8), different from that of pristine $BiVO_4$ (Supplementary Fig. 9). The PEC performance of $Nb_2O_5/BiVO_4$ after potentiostatic polarization in an electrolyte containing various concentrations of Cl^- indicates its extensive applicability (Supplementary Fig. 10). In the X-ray absorption near-edge structure region and extended X-ray absorption fine-structure (EXAFS) spectroscopy analysis (Supplementary Figs. 11 and 12), the absorption edge of $Nb_2O_5/BiVO_4$ is close to that of Nb_2O_5, indicating that Nb exists as Nb^{5+}. The Nb K-edge obtained by X-ray absorption near-edge structure valence fitting indicates that Nb^{3+} predominantly presents in $NbClO_x/BiVO_4$ (Supplementary Fig. 13)[29]. The Fourier-transformed EXAFS spectrum (*R*-space) shows a new peak at 2.1 Å on $NbClO_x/BiVO_4$ (Fig. 1f), ascribed to the contribution of Nb–Cl coordination, where one Nb atom is coordinated with ~4.4 Cl atoms (Supplementary Table 1). In the wavelet-transformed EXAFS (Supplementary Fig. 14), the major intensity maximums at 3.9 A^{-1} and 4.7 A^{-1} are attributed to Nb–O and Nb–Cl bonds[30] in $Nb_2O_5/BiVO_4$ and $NbClO_x/BiVO_4$, respectively. In addition, the peak intensity of Cl 2*p* in the X-ray photoelectron spectroscopy (XPS) spectrum increases with the potentiostatic polarization time (Fig. 1g), with the characteristic peaks at 199.6 eV and 198 eV corresponding to Cl^- species (Supplementary Fig. 15)[31]. The high-valence chlorine of ClO^- is also observed at 200.3 eV and 201.8 eV for Cl $2p_{3/2}$ and $2p_{1/2}$ peaks, respectively, which are assigned to the surface reaction product of the photoelectrode (ClO^-). The Bi 4*f* and V 2*p* peaks shift towards high binding energy, while the Nb 3*d* peak shifts to low binding energy with the polarization time (Supplementary Fig. 16 and Supplementary Note 5), demonstrating the influence of electronic structure from Nb species and electron transfer between the catalyst and the semiconductor during the Cl^- insertion process.

We confirmed the Cl^- insertion into Nb_2O_5 through in situ attenuated total reflection Fourier transform infrared spectroscopy with the OTTO configuration (ATR-FTIR OTTO) analysis (Supplementary Fig. 17). The peaks at 867 and 912 cm^{-1} attributed to ClO^- increase with measuring time (Supplementary Fig. 18), which proves that the insertion of Cl^- into Nb_2O_5 enhances the oxidation kinetics on $Nb_2O_5/BiVO_4$. PEC measurement on $NbClO_x/BiVO_4$ after potentiostatic polarization was performed in a Cl^--free electrolyte (0.5 M Na_2SO_4) (Supplementary Fig. 19 and Supplementary Note 6). A weak ClO^- signal is captured by in situ ATR-FTIR OTTO (Fig. 1h), suggesting that Cl^- in $NbClO_x$ participates in the AC synthesis process.

The PEC performances of $NbClO_x/BiVO_4$ were evaluated for direct AC synthesis from natural seawater (Supplementary Fig. 20). The optimized sample exhibits a photocurrent density of 6.26 mA cm^{-2} at 1.72 V_{RHE}, with an applied bias photon-to-current efficiency of 2.41%, remarkably higher than that of $BiVO_4$ (2.43 mA cm^{-2}; 0.59%) (Fig. 1i and Supplementary Fig. 21). The onset potential of $NbClO_x/BiVO_4$ is 0.6 V_{RHE}, which is substantially lower than the theoretical synthesis potential of ClO^- (1.72 V_{RHE}), stemming from the considerable photovoltage (Supplementary Fig. 22). We also evaluated the performance of $NbClO_x/BiVO_4$ under natural sunlight, and the obtained result is consistent with that under simulated sunlight, confirming the reliability of the result (Supplementary Fig. 23). The outstanding performances are considerably superior to those of state-of-the-art ClOR electrosynthesis electrodes (Supplementary Tables 2–8, Supplementary Figs. 24–33 and Supplementary Notes 7 and 8), demonstrating the potential advantage of PEC ClOR. The ClO^- FEs and yields on $NbClO_x/BiVO_4$ and $BiVO_4$ depend on the photocurrent densities at various potentials (Supplementary Fig. 34). $NbClO_x/BiVO_4$ exhibits ClO^- FEs and selectivities of more than 95% over a wide potential range from 1.2 to 1.8 V_{RHE}, noticeably higher than those of $BiVO_4$ (Fig. 1j and Supplementary Fig. 35). Its ClO^- yield is 116.3 µmol cm^{-2} h^{-1} at 1.72 V_{RHE} for ClO^- synthesis, 3.19 times as large as that of $BiVO_4$ (36.5 µmol cm^{-2} h^{-1}). $NbClO_x/BiVO_4$ also maintains 95.58% of the initial current over 180 h at 1.3 V_{RHE} in natural seawater, while $BiVO_4$ displays an obvious decay in photoresponse within 18 h (Fig. 1k). This suggests that the $NbClO_x$ catalyst considerably improves the seawater corrosion resistance of $BiVO_4$.

Direct synthesis of disinfectants from seawater

Long-term concentration accumulation is one of the most important indicators of industrially produced disinfectants. We performed concentration accumulation of disinfectants on $NbClO_x/BiVO_4$ with a size of 1 cm^2 in natural seawater (100 ml; initial pH, 8.06) at 1.3 V_{RHE} over time (Supplementary Figs. 36 and 37). The seawater pH decreases from 8.06 to 3.97 after 10 h during the disinfectant synthesis ($Cl^- + 2OH^- \rightarrow ClO^- + H_2O + 2e^-$). The ClO^- accumulated concentration reaches a value of 95.33 ppm after 3 h, followed by gradual decay until 10 h owing to the accelerated decomposition of ClO^- in acidic environments. As the pH is stabilized at 8.06, the accumulated concentration of the disinfectant essentially increases over time, up to 272.91 ppm within 10 h. Regulating the pH of the threshold electrolyte offers the possibility of synthesizing highly concentrated disinfectants.

Following *J*–*V* measurements, the photocurrent density and ClO^- FE were analysed and quantified (Supplementary Fig. 38). Heat maps intuitively display the relationship of photocurrent density and ClO^- FE dependence on pH and applied potential on $NbClO_x/BiVO_4$ in seawater (Fig. 2a,b). $NbClO_x/BiVO_4$ shows a high photocurrent density at low voltages in acidic seawater, which remains consistent from pH 3 to 11 as the potential is higher than 1.4 V_{RHE}. The applied bias photon-to-current efficiency values display a decreased trend with increasing pH (Supplementary Fig. 39 and Supplementary Table 9). $NbClO_x/BiVO_4$ maintains a ClO^- FE above 70% for 22 h at pH 10, much higher than those at other pH values (Fig. 2b). The decrease in FE over time is due to the cumulative inhibition of ClOR by ClO^- concentration. Meanwhile, the ClO^- content increases with time at pH 6–11 in seawater, reaching a concentration of 550.40 ppm by 22 h under 1.3 V_{RHE} at pH 10

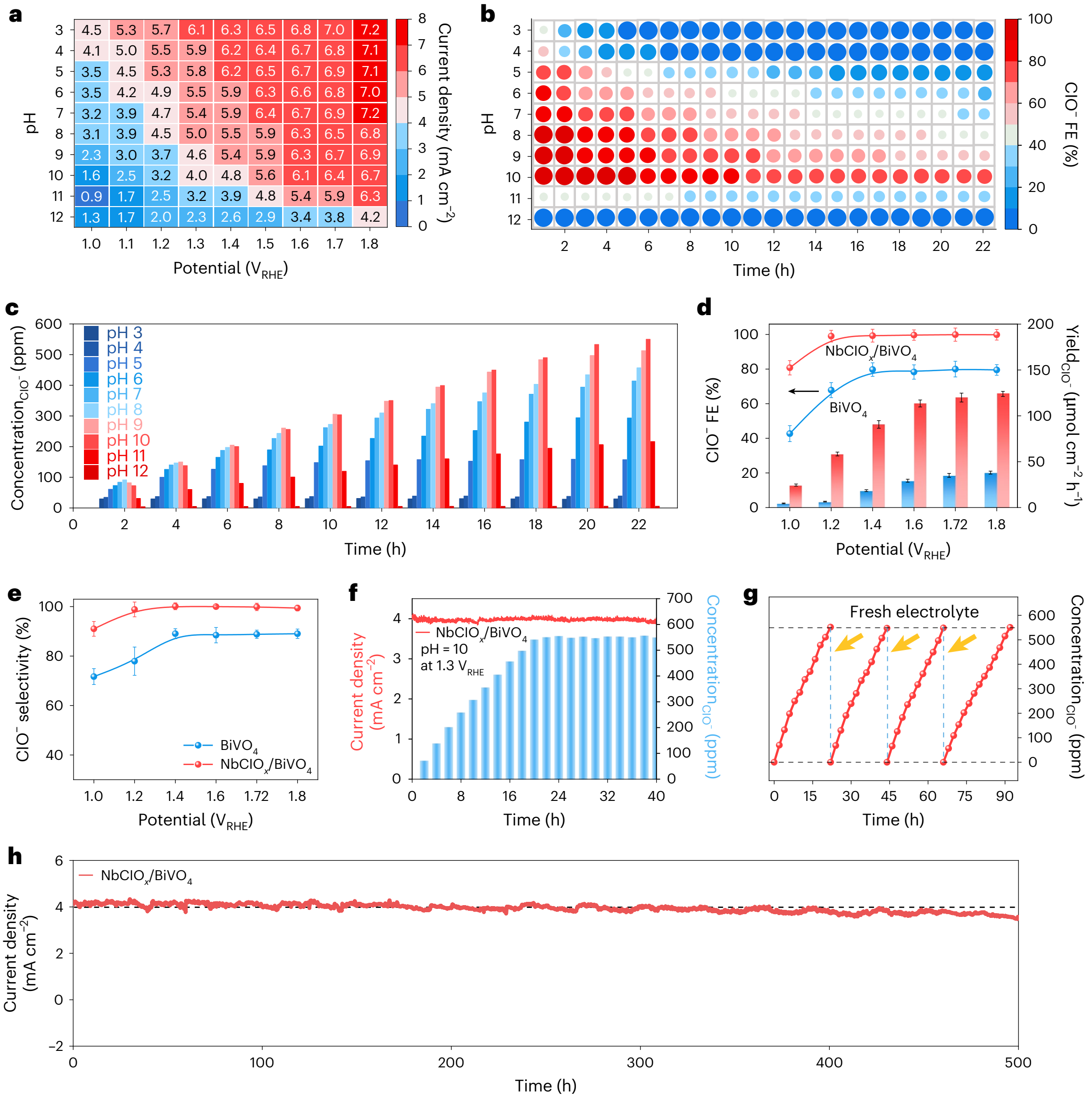

pH	1.0	1.1	1.2	1.3	1.4	1.5	1.6	1.7	1.8
3	4.5	5.3	5.7	6.1	6.3	6.5	6.8	7.0	7.2
4	4.1	5.0	5.5	5.9	6.2	6.4	6.7	6.8	7.1
5	3.5	4.5	5.3	5.8	6.2	6.5	6.7	6.9	7.1
6	3.5	4.2	4.9	5.5	5.9	6.3	6.6	6.8	7.0
7	3.2	3.9	4.7	5.4	5.9	6.4	6.7	6.9	7.2
8	3.1	3.9	4.5	5.0	5.5	5.9	6.3	6.5	6.8
9	2.3	3.0	3.7	4.6	5.4	5.9	6.3	6.7	6.9
10	1.6	2.5	3.2	4.0	4.8	5.6	6.1	6.4	6.7
11	0.9	1.7	2.5	3.2	3.9	4.8	5.4	5.9	6.3
12	1.3	1.7	2.0	2.3	2.6	2.9	3.4	3.8	4.2

Fig. 2 | Long-term PEC stability of $NbClO_x/BiVO_4$ in natural seawater with regulated pH. a, Heat map of current density corresponding to $NbClO_x/BiVO_4$ at different voltages with various pH levels. **b**,**c**, FE heat map for ClO^- (**b**) and accumulated concentration of $NbClO_x/BiVO_4$ at various times for long-term measurements at different pH levels at 1.3 V_{RHE} (**c**). **d**,**e**, FE, yield (**d**) and selectivity (**e**) of ClO^- of $NbClO_x/BiVO_4$ in seawater at pH = 10. The bars/balls in **d** and **e** represent the mean value for $n = 3$ experiments and data distribution is represented by the dots. **f**, *J*–*t* curve and ClO^- accumulation concentrations for a 40-h stability test of $NbClO_x/BiVO_4$. **g**, Cycling tests of $NbClO_x/BiVO_4$ for ClO^- accumulation concentrations. The arrows indicate replacement with fresh seawater electrolyte. **h**, 500 h of operation on $NbClO_x/BiVO_4$ at 1.3 V_{RHE} in seawater (pH = 10).

(Fig. 2c and Supplementary Table 10), in agreement with the demand for conventional disinfection. Ultimately, $NbClO_x/BiVO_4$ exhibits ClO^- FEs and selectivities near 100% in the potential range of 1.2–1.8 V_{RHE} at pH 10 in seawater (Fig. 2d,e and Supplementary Fig. 40). Note that at 1.72 V_{RHE}, a FE of 99.9 ± 3% and a yield of 119.9 µmol cm^{-2} h^{-1} are achieved (Fig. 2d). We conducted preliminary life cycle assessment and basic economic analysis, and compared the $NbClO_x/BiVO_4$ photoanode with a commercially available dimensionally stabilized anode (DSA) in the chlor-alkali industry using a two-electrode system (Supplementary Fig. 41 and Supplementary Notes 9 and 10). The production of the same amount of ClO^- on $NbClO_x/BiVO_4$ reduces electricity costs by 77.16% and CO_2 emissions by 75.31% (traditional grid) in comparison with the DSA electrode (Supplementary Figs. 42–44 and Supplementary Tables 11–15). On the basis of the price of renewable electricity (US\$0.03 kWh^{-1}), the cost of producing ClO^- is calculated as US\$0.042 ± 0.003 kg^{-1}, well below the current commercial rates[32].

Next, we measured the ClO^- concentration accumulation on $NbClO_x/BiVO_4$ (1 cm^2) in seawater (100 ml, pH = 10) at 1.3 V_{RHE}. The ClO^- concentration remains essentially invariable after 22 h owing to the ClO^- saturation (Fig. 2f). We subsequently assessed the continuous disinfectant synthesis on $NbClO_x/BiVO_4$ through 22 h per cycle. As expected, it produces over 400 ml of disinfectant with a concentration exceeding 550 ppm after four cycles within 92 h (Fig. 2g). The stability of $NbClO_x/BiVO_4$ is maintained over 500 h in seawater (pH = 10) after chronoamperometric measurement (Fig. 2h), representing the best stability record for PEC synthesis of value-added products in seawater conditions. The scanning electron microscopy images taken after 500 h exhibit a change in surface morphology compared with the one before stability (Supplementary Figs. 45 and 46). A slight decrease in the X-ray diffraction (XRD) peak intensity of $NbClO_x/BiVO_4$ is also observed (Supplementary Fig. 47), which is ascribed to the thickening of the uniform amorphous $NbClO_x$ layer (~7 nm) (Supplementary Fig. 48).

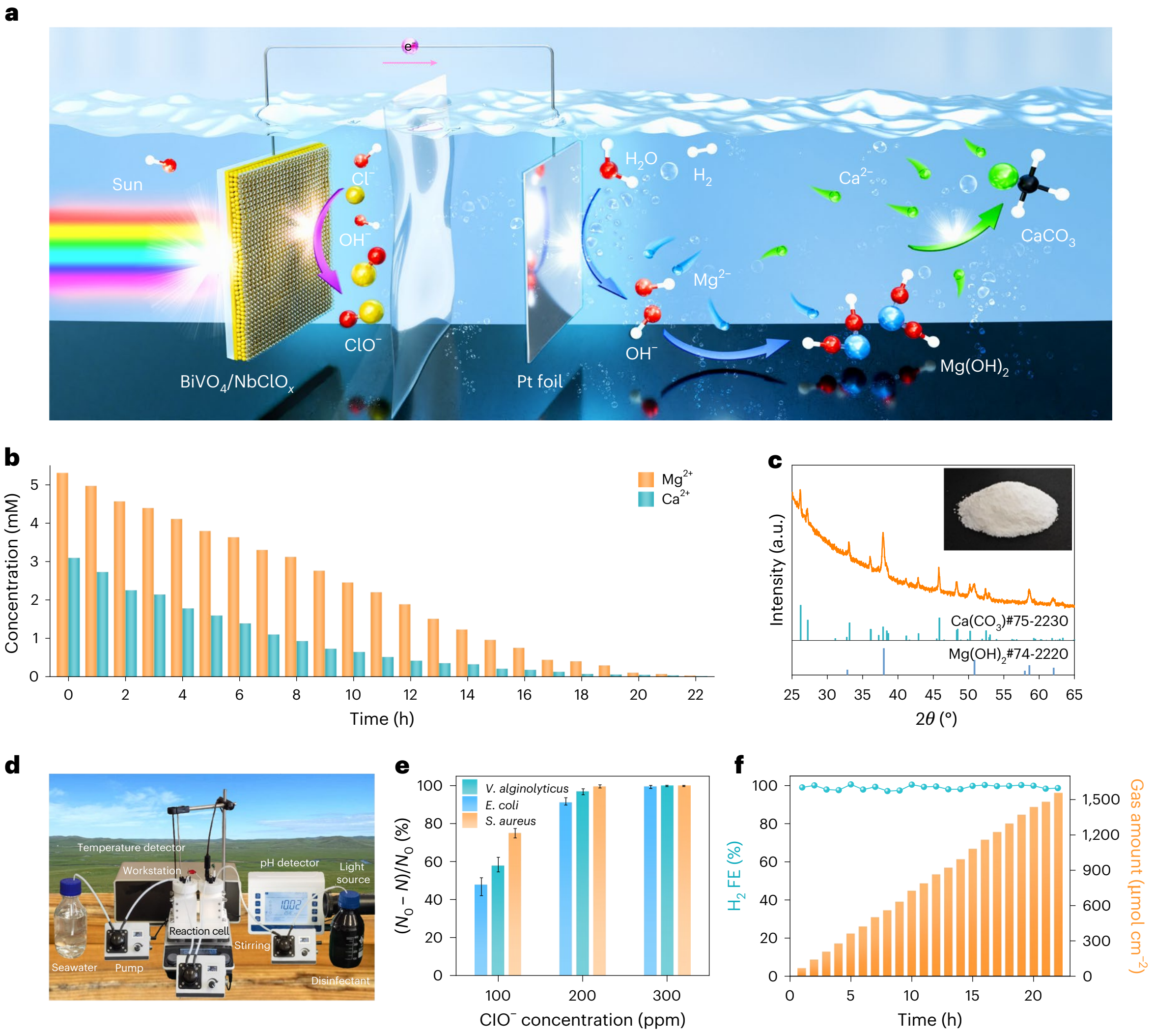

Fig. 3 | Synthesis of value-added products from natural seawater cathodes. **a**, Anodic and cathodic products of seawater (pH = 10). **b**, Concentrations of alkali metal ions in seawater at various times. **c**, XRD pattern of the cathode product. The inset shows a digital image of the product. **d**, Simulated industrial tandem reaction device. **e**, Photoelectrochemical synthesis of sterilization at various disinfectant concentrations. The bars represent the mean value for $n = 3$ experiments. **f**, Hydrogen contents and FEs over 22 h.

Moreover, increased peak intensities of O_{OH} (hydroxyl oxygen) and ClO^- are found in XPS spectra (Supplementary Fig. 49), which indicates that the substantial hydroxyl adsorbed on the surface is favourable for the formation of ClO^-. No Ca 2*p* or Mg 1*s* XPS peaks are detected after testing, suggesting that chloride mediation effectively inhibits Ca^{2+} and Mg^{2+} covering on the photoanode surface.

Synthesis of other value-added products

Diverse cations in seawater, such as Mg^{2+}, Ca^{2+} and Na^+, facilitate the simultaneous creation of high-value products and hydrogen through strategy design[33]. We used an H-type electrolytic cell with an $NbClO_x/BiVO_4$ anode and a standard Pt cathode to monitor the reaction process. We added 100 ml of natural seawater to the cathode and anode chambers separately (Fig. 3a), and the disinfectant was produced at the anode. At the cathode side, the Mg^{2+} and Ca^{2+} concentrations decrease over time according to ion chromatography analysis, from the initial 5.30 mM (Mg^{2+}) and 3.10 mM (Ca^{2+}) to 0.05 mM (Mg^{2+}) and 0.03 mM (Ca^{2+}) after 22 h, respectively (Fig. 3b, Supplementary Fig. 50 and Supplementary Table 16), implying the effective removal of alkaline earth metal ions from seawater. Concurrently, the precipitates covering the cathode include the products $CaCO_3$ (JCPDS: 75-2230) and $Mg(OH)_2$ (JCPDS: 74-2220) (Fig. 3c). The cathode generates a large quantity of OH^- ions during the reaction process ($2H_2O + 2e^- \rightarrow 2OH^- + 2H_2$), which combine with Mg^{2+} ions to form $Mg(OH)_2$. Simultaneously, the increased seawater pH causes a decrease in the solubility and precipitation of Ca^{2+} and CO_3^{2-}.

A tandem device capable of continuous synthesis of disinfectant was designed, employing $NbClO_x/BiVO_4$ (1 cm^2) as the anode and Pt sheet (1 cm^2) as the cathode. As illustrated in Fig. 3d, the reaction was driven by simulated sunlight (AM 1.5 G, 100 mW cm^{-2}) and an applied potential of 1.3 V_{RHE}, with a peristaltic pump introducing the seawater to the reaction cell. The cathodic half-reaction obtains hydrogen during the removal of Ca^{2+} and Mg^{2+}, and then the softened seawater is pumped into the anodic reaction cell. Finally, the disinfectant produced at the anode is transferred to a 100-ml brown bottle by a peristaltic pump. Within 22 h, this tandem device can generate disinfectants at concentrations above 550 ppm at the anode and value-added $Mg(OH)_2$, $CaCO_3$ and hydrogen at the cathode. We next performed disinfection measurements on representative pathogenic bacteria (for example, *Staphylococcus aureus*, *Escherichia coli* and *Vibrio alginolyticus*[34,35]), and seawater was used as a control experiment (Supplementary Fig. 51). Bacteria were incubated in seawater containing various AC

https://doi.org/10.1038/s41893-025-01530-y

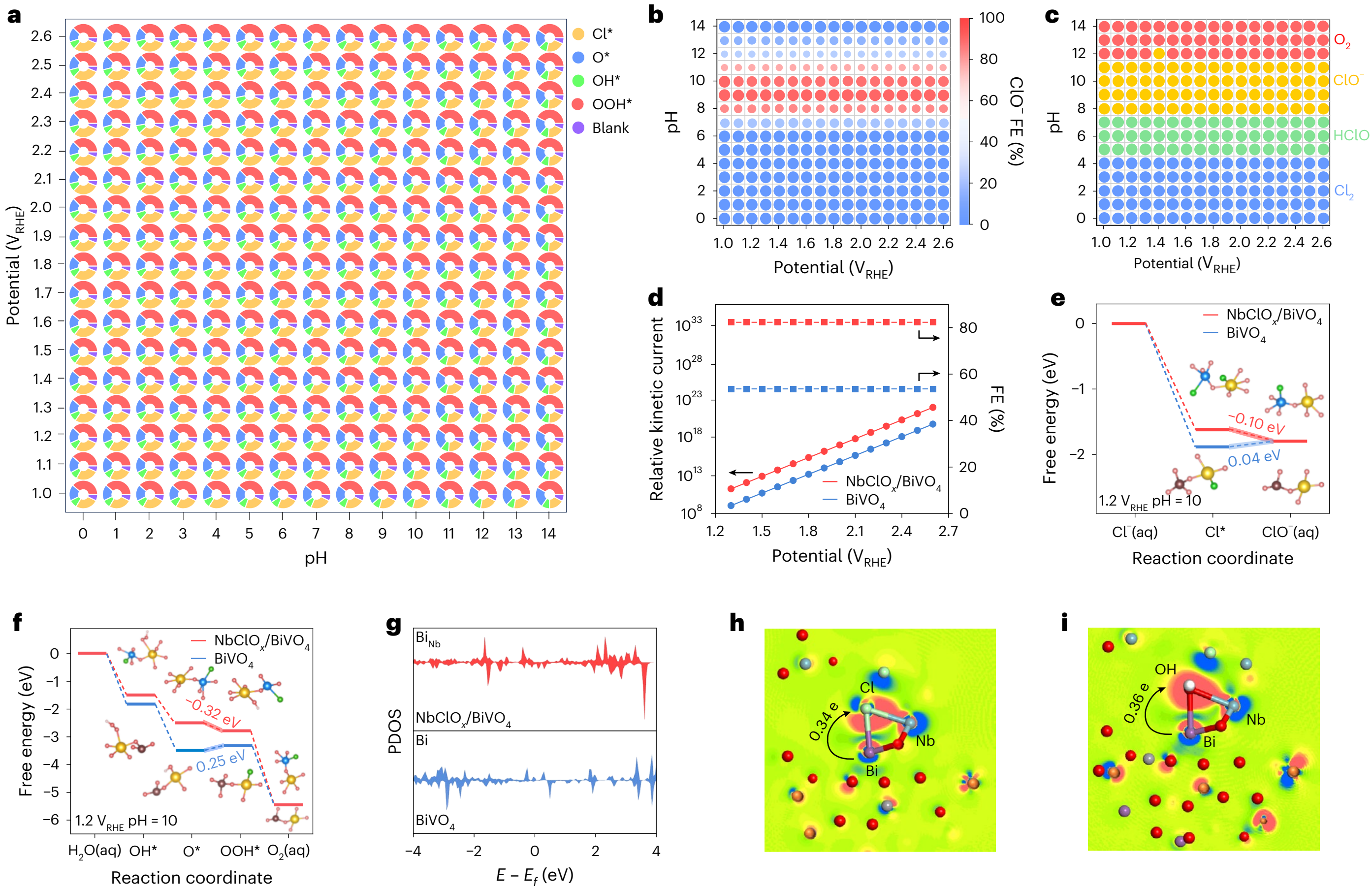

Fig. 4 | Theoretical calculations of ClOR for $NbClO_x/BiVO_4$ and $BiVO_4$. **a**–**c**, The pH and potential dependence of adsorbate coverage (**a**), ClO^- FE (**b**) and products (**c**). **d**, Relative kinetic current and FE chart calculated at pH = 10 using a microkinetic model. **e**,**f**, Active sites and free energy diagrams on $NbClO_x/BiVO_4$ and $BiVO_4$. The measurements were taken at pH = 10 and $U = 1.2\ V_{RHE}$. **g**, Projected density of states (PDOS) of Bi active sites. *E*, electron orbital energy; E_f, Fermi level. **h**,**i**, Charge density contour maps of $NbClO_x/BiVO_4$ adsorbed Cl* (**h**) and OH* (**i**). e, electron. The red, green, brown, white, grey and purple spheres represent O, Cl, V, H, Nb and Bi atoms, respectively.

concentrations for three days. The sterilization rate is ~100% for all bacteria at AC concentrations above 300 ppm (Fig. 3e), demonstrating the feasibility of PEC synthetic disinfectant application. Furthermore, the generated H_2 accumulates to 1,554.8 μmol cm^{-2} in 22 h with a FE close to 100% (Fig. 3f, Supplementary Fig. 52 and Supplementary Table 17).

Theoretical simulations

Machine learning potential energy molecular simulations and first-principles methods were implemented to investigate OER and ClOR intermediate adsorption energies on $NbClO_x/BiVO_4$ and $BiVO_4$ (refs. 36,37). Two processes involve the $NbClO_x/BiVO_4$ interface and Cl^- insertion, resulting in a low-symmetry structure. Each site's free energy diagram was calculated using the computational hydrogen electrode method (Supplementary Tables 18–21). We obtain the relationship between potential and pH-dependent adsorbate distributions (Fig. 4a), denoting that O species (mainly OOH* and OH*) and Cl species (mainly Cl*) appear simultaneously at most potentials, with different sites adsorbing different adsorbates. In general, Cl* species increase with increasing potential. The adsorption of Cl* decreases with growing pH, and the main adsorbed species are OOH* and O* at pH > 12. Subsequently, the high activity and FE of $NbClO_x/BiVO_4$ were investigated via microkinetic modelling, and correlations of the FEs and main products of the ClOR process were calculated with different pHs and potentials. $NbClO_x/BiVO_4$ has high FEs above 80% at pH = 8–10 (Fig. 4b), while the main products are dominated by Cl_2, AC and O_2 at pH < 5, pH = 5–11 and pH > 11 (Fig. 4c), respectively. The electrocatalytic reactions on $NbClO_x/BiVO_4$ and $BiVO_4$ were simulated, and the kinetic currents and FEs of the microkinetic models at pH = 10 were compared (Fig. 4d). This reveals that the electrocatalytic activity of $NbClO_x/BiVO_4$ is superior to that of $BiVO_4$, and the ClOR FEs on $NbClO_x/BiVO_4$ and $BiVO_4$ are 83% and 56%, respectively, which match with the experimental results. In addition, isotopic labelling tests show that the O in ClO^- comes from the adsorptive transformation of hydrolytic dissociated OH^- on the $NbClO_x/BiVO_4$ surface (Supplementary Fig. 53 and Supplementary Note 11).

Machine learning potential energy calculation of nearly 300 sites for $NbClO_x/BiVO_4$ and $BiVO_4$ was conducted to determine the optimal active site and the free energy diagram. The active site of $NbClO_x/BiVO_4$ is Bi bonded to Nb (Bi_{Nb}) at the interface, with stronger adsorption of Cl* than OH*, which leads to better ClOR selectivity than OER (Fig. 4e,f). The active sites at the interface of $NbClO_x$ and $BiVO_4$ enhance the transfer efficiency of photogenerated charge carriers involved in the surface oxidation reaction. In addition, the conventional Bi sites in $BiVO_4$ have a higher projected density of states near the Fermi level than $NbClO_x/BiVO_4$ (Fig. 4g), allowing stronger adsorption of OH* and Cl* intermediates, which reduces the reactivity (ClOR is limited by the desorption rate). The highly active O species on the $BiVO_4$ surface also reduce the ClO^- FE. After the adsorption of Cl^- and OH^- on $NbClO_x/BiVO_4$, charge transfers from Bi_{Nb} sites to Cl^- (0.34 eV) and OH^- (0.36 eV) (Fig. 4h,i) are superior to those from Bi sites of $BiVO_4$ to Cl^- (0.28 eV) and OH^- (0.24 eV) (Supplementary Fig. 54). These results indicate that the

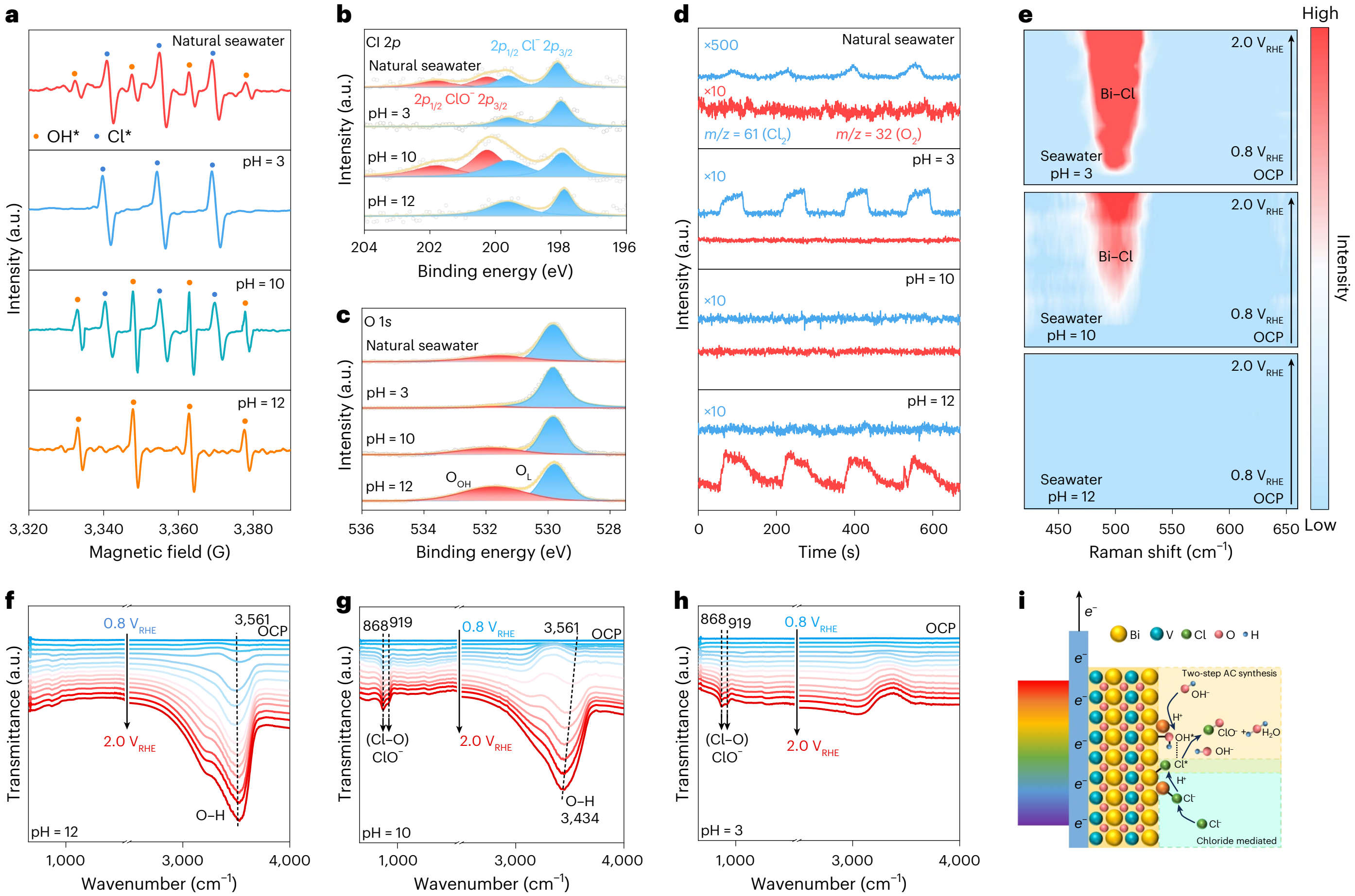

Fig. 5 | Mechanistic study of disinfectant synthesis on $NbClO_x/BiVO_4$. **a**, PEC quasi in situ EPR tests. **b**,**c**, Quasi in situ XPS of Cl 2*p* (**b**) and O 1*s* (**c**). **d**, PEC online DEMS results for the disinfectant. EPR, XPS and DEMS were performed at 1.3 V_{RHE} under AM 1.5 G illumination. **e**, Colour map representations of in situ Raman spectra intensities on $NbClO_x/BiVO_4$ in seawater at various pH values. OCP represents open circuit potential. **f**–**h**, In situ ATR-FTIR OTTO of $NbClO_x/BiVO_4$ in seawater at pH = 12 (**f**), pH = 10 (**g**) and pH = 3 (**h**). **i**, Two-step AC synthesis of $NbClO_x/BiVO_4$ in a seawater system.

Bi_{Nb} sites increase the electrophilicity of Cl^- and OH^- activation, which is favourable for the reaction activity.

Reaction mechanism

Quasi in situ electron paramagnetic resonance (EPR) was carried out to monitor the $NbClO_x/BiVO_4$ surface reaction intermediates during the PEC process (Supplementary Fig. 55). The electrolyte condition depends on the types of intermediates in the sample. As shown in Fig. 5a, only Cl* or OH* signals are found in acidic (pH = 3) or strongly alkaline (pH = 12) seawater, respectively. Both Cl* and OH* are captured in weakly alkaline (pH = 10) and natural seawater, and a stronger OH* signal intensity appears in weakly alkaline seawater than in natural seawater, offering the possibility of avoiding the occurrence of the Heyrovsky step. Quasi in situ XPS analysis (Fig. 5b and Supplementary Fig. 56) verifies that no ClO^- signal is detectable in acidic or strongly alkaline seawater, while the ClO^- peak is prominent for the sample in weakly alkaline seawater, evidencing its highly selective ClO^- synthesis. The O_{OH} peak in the O 1*s* spectrum increases with rising pH (Fig. 5c). The product compositions on $NbClO_x/BiVO_4$ were further examined through PEC online differential electrochemical mass spectrometry (DEMS) (Supplementary Fig. 57). The product compositions are 61 and 32 *m*/*z* signals for Cl_2 and O_2, respectively, and these signals are prominently discerned in both acidic and alkaline seawater (Fig. 5d). In natural seawater, a very weak Cl_2 signal is detected with no O_2 signal, while no Cl_2 and no O_2 are observed in weakly alkaline seawater. An obvious O_2 signal is present for the pristine $BiVO_4$ in weakly alkaline seawater (Supplementary Fig. 58), suggesting the OER process taking place at the surface. In contrast, the chlorine-mediated $NbClO_x/BiVO_4$ allows for the conversion of OH* and Cl* to ClO^-, consistent with the above calculations.

In situ Raman spectrum and in situ ATR-FTIR OTTO were performed to capture possible intermediates and explore reaction pathways on the $NbClO_x/BiVO_4$ electrode (Supplementary Fig. 59). The Raman spectrum shows the typical characteristic peaks of VO_4^{3-} (329 and 366 cm^{-1}) and V–O (714 and 822 cm^{-1}) (Supplementary Fig. 60)[38]. A notable Bi–Cl stretching vibration (502 cm^{-1}) is observed with decreasing seawater OH^- concentration and increasing potential (Fig. 5e and Supplementary Fig. 61), showing that various OH^- concentrations in seawater modulate the reaction intermediates on the $NbClO_x/BiVO_4$ surface. Although the Raman stretching vibration of O–H at 715 cm^{-1} overlaps with the V–O bond, the O–H signal at 3,561 cm^{-1} and the Cl–O characteristic peaks at 868 and 919 cm^{-1} representing ClO^- are successfully captured by in situ ATR-FTIR OTTO (Fig. 5f–h)[39]. The characteristic peaks of O–H gradually increase with increasing pH. In weakly alkaline seawater, the Cl–O bond is enhanced with growing potential, and the O–H peak shifts negatively from 3,561 to 3,434 cm^{-1} (Fig. 5g), which is associated with the kinetic effect induced by the coupling process and chemical reaction of the Cl* and OH* intermediates[40]. Weak Cl–O signals are detected at potentials above 1.5 V_{RHE} in acidic seawater, which is ascribed to the dissolution of Cl_2 (Fig. 5h). More substantial Cl–O characteristic peaks are observed in weakly alkaline seawater, and no Cl–O signals are discerned in strongly alkaline seawater (Fig. 5f), implying that weakly alkaline seawater is favourable for AC selective synthesis (Supplementary Fig. 62). In situ Raman spectroscopy shows stronger adsorption of Cl* on $BiVO_4$ in seawater than on $NbClO_x/BiVO_4$ in weakly alkaline seawater (Supplementary Fig. 63). In situ ATR-FTIR OTTO successfully captured OH* and OOH* species on the surface of $BiVO_4$ (Supplementary Fig. 64). We deduce that strong adsorption of Cl* by $BiVO_4$ makes it difficult to desorb, resulting in chlorine poisoning, while the highly reactive oxygen species on its surface promote the OER process, leading to a lower FE for AC synthesis (Supplementary Fig. 65). The above analyses demonstrate that the chlorine-mediated effect on $NbClO_x/BiVO_4$ inhibits the adsorption of Cl* by $BiVO_4$, preferring the reaction step $Cl^* + OH^* + OH^-(aq) \rightarrow ClO^* + H_2O + e^-$ in weak alkaline seawater (Fig. 5i, Supplementary Fig. 66 and Supplementary Note 12), avoiding the generation of Cl_2.

Discussion

Our work shows a two-step synthesis of disinfectants from seawater on the $NbClO_x/BiVO_4$ photoelectrode without Cl_2 release, while obtaining value-added products, including $CaCO_3$, $Mg(OH)_2$ and H_2. $NbClO_x/BiVO_4$ has an onset potential of 0.6 V_{RHE}, with FEs of AC approaching 100% at 1.2–1.8 V_{RHE} and a yield of 119.9 μmol cm^{-2} h^{-1} at 1.72 V_{RHE}. Synthesizing the same amount of ClO^- on this photoelectrode reduces electricity costs by 77.16% and CO_2 emissions by 75.31% in comparison with the commercial DSA, and the cost of ClO^- is estimated to be approximately \$0.042 ± 0.003 kg^{-1}. The adsorption and conversion of OH* and Cl* species are the key to the reaction steps, and the chlorine-mediated behaviour of $NbClO_x/BiVO_4$ has been demonstrated. Our work advances the synthesis of disinfectants and the utilization of seawater resources towards higher sustainability. The molecular-level understanding of this two-step synthesis process may inspire more studies on chlorine-activated intermediate-driven transfer reactions.

Methods

Preparation of the $BiVO_4$ photoanode

In a typical procedure for the synthesis of $BiVO_4$ (ref. 26), a 0.4 M KI (Alfa Aesar) solution was adjusted to a pH of 1.7 by adding HNO_3 (Sinopharm Chemical Reagent). Subsequently, 0.04 M $Bi(NO_3)_3{\cdot}5H_2O$ (Alfa Aesar) was added and fully dissolved before electrodeposition. The electrodeposition was carried out at −0.1 $V_{Ag/AgCl}$ for 60, 120, 180, 240 and 300 s at room temperature using a three-electrode system to form BiOI. Then, 0.2 M $VO(acac)_2$ (Alfa Aesar) dissolved in dimethyl sulfoxide was dropped onto the BiOI film, followed by annealing at 450 °C for 2 h to form the $BiVO_4$ photoanode. The annealed $BiVO_4$ was then immersed in 1 M NaOH (Sinopharm Chemical Reagent) for 20 min to remove excess V_2O_5 on the top surface. Finally, the photoanode was rinsed with deionized water and dried in air.

Preparation of the $NbClO_x/BiVO_4$ and $Nb_2O_5/BiVO_4$ photoanodes

$BiVO_4$ photoanodes were electrodeposited in aqueous solutions containing various concentrations of ammonium niobate(V) oxalate hydrate (Alfa Aesar) (0.005, 0.05 and 0.5 mM) at −0.3 $V_{Ag/AgCl}$ for 2 h. The samples were then annealed in an argon atmosphere at various temperatures (250, 350 and 450 °C) for 1 h. The corresponding samples were labelled as $Nb_2O_5/BiVO_4$. The $Nb_2O_5/BiVO_4$ photoanodes were subjected to potentiostatic polarization in 0.5 M NaCl at various potentials (0.8, 1.0, 1.2 and 1.4 V_{RHE}) for 1 h under AM 1.5 G illumination (100 mW cm^{-2}, XES-40S3-TT, AAA Class Solar Simulator, Japan) for the formation of $NbClO_x/BiVO_4$. A commercial DSA, RuO_2–TiO_2, was purchased from Suzhou Shuertai Industrial Technology Co.

Photoelectrochemical measurements

Photoelectrochemical measurements were carried out using an electrochemical workstation (CHI760D). A typical three-electrode H-type cell was used, consisting of photoanodes as the working electrode, an Ag/AgCl electrode (in saturated KCl solution) as the reference electrode and a platinum sheet as the counter electrode, with untreated natural seawater as the electrolyte. The cell was divided into a cathode compartment (100 ml) and an anode compartment (100 ml) by an anion exchange membrane (Nafion 117). No IR correction was applied in this work. All electrochemical data were repeated more than three times, with error bars representing the standard deviation of the data. All potentials were calibrated to the RHE using equation (1):

$$E_{\mathrm{RHE}} = E_{\mathrm{Ag/AgCl}} + 0.0591 \times \mathrm{pH} + \varphi_{\mathrm{reference}} \tag{1}$$

Determination and quantification of ClO^- using UV–Vis spectroscopy

ClO^- concentrations were determined and quantified using UV–Vis spectroscopy (UV–2600, Shimadzu) through the o-tolidine method. The concentration of ClO^- was measured at scheduled intervals at various potentials (1.0–1.8 V_{RHE}). A certain amount of the electrolyte was taken from the electrolysis cell and diluted to 10 ml within the detection range, and then 0.5 ml of o-tolidine solution (1 g l^{-1} o-tolidine, pH adjusted to 0 with hydrochloric acid) was added. The absorption spectrum was measured after 1 min, and the absorption intensity was recorded at 437.5 nm. The standard concentration–absorbance curve was calibrated using a standard solution of sodium hypochlorite (concentration 0.1 mol l^{-1}). The FE of ClO^- was calculated using equation (2):

$$\mathrm{FE}_{\mathrm{ClO^-}} = \frac{Q_{\mathrm{ClO^-}}}{Q} = \frac{n_{\mathrm{ClO^-}} \times V \times C_{\mathrm{ClO^-}} \times F}{Q} \tag{2}$$

where Q is the total coulombs (C) applied during the test, Q_{ClO^-} is the coulombs required to produce ClO^-, n is the number of electrons transferred (2 for ClO^-), V is the volume of the anode solution in the anode chamber (100 ml), C_{ClO^-} is the concentration of ClO^- produced and F is the Faraday constant (96,485 C mol^{-1}).

The formulae for calculating ClO^- selectivity and yield rate are as follows:

$$\mathrm{ClO}^-_{\mathrm{selectivity}} = \frac{(\text{content of corresponding product})}{(\text{consumption of reactant})} \times 100\% \tag{3}$$

$$\mathrm{ClO}^-_{\text{yield rate}} = \frac{(\text{productivity of products})}{(t \times A)} \tag{4}$$

where t represents the time (s), and A represents the photoelectrode area (cm^2).

Stability and cycling of $NbClO_x/BiVO_4$

Long-term stability tests of the $NbClO_x/BiVO_4$ electrode were performed with an H-type electrolytic cell, in which the working electrode was a $NbClO_x/BiVO_4$ (1 cm^2) photoanode, the reference electrode was Ag/AgCl and the counter electrode was a platinum sheet. At 1.23 V_{RHE} under AM 1.5 G illumination, 100 ml of seawater (pH = 10) was added to both cells, with the photoanode and reference electrode on the same side of the electrolytic cell, and the counter electrode on the opposite side. During the test, the stirring rate was maintained at 200 rpm. The ClO^- concentration in the seawater was measured at 1-h intervals. The reaction electrolyte was extracted every 22 h using a peristaltic pump and replaced with fresh seawater (pH = 10).

DEMS

The electrolyte (seawater at various pH levels) was fed into a custom DEMS (Linglu, QAS 100) photoelectrochemical cell using a peristaltic pump. Using Cl_2 and O_2 as probe molecules allowed for the ultra-close-range (less than 5 μm) specific detection of Cl_2 and O_2 generated on the surface of the photoanode. Simulated sunlight (100 mW cm^{-2}) was alternately applied with an interval of 100 s at a constant potential of 1.2 V_{RHE}. The next cycle commenced after the electrochemical test concluded and the mass signal returned to baseline, and the experiment concluded after four cycles.

Quasi in situ EPR measurements

Quasi in situ EPR (Bruker, EXM plus) measurements were conducted using 5,5-dimethyl-1-pyrroline *N*-oxide (DMPO) as a spin-trapping agent to capture surface-adsorbed species potentially generated during the photoelectrochemical process. Photoelectrochemical reactions were carried out in seawater at various pH values at 1.3 V_{RHE} under simulated sunlight (100 mW cm^{-2}) to capture these adsorbates. After 60 s of reaction, 100 μl of 0.2 M DMPO solution was added to the photoanode, ensuring close contact between DMPO and the photoanode. EPR measurements were swiftly performed with the following parameters: frequency, 9.412911 GHz; modulation amplitude, 1 G; microwave power, 10.00 mW; scan width, 100 G.

Photoelectrochemical in situ Raman tests

Photoelectrochemical in situ Raman measurements were performed via micro confocal Raman spectroscopy (Renishaw inVia Spectrometer System using visible excitation at 532 nm) and an electrochemical workstation. The H-type cell, made of polytetrafluoroethylene, has a quartz window between the sample and the objective lens, and a quartz window at the back of the cell for light transmission. The Raman was equipped with a flexible arm for signal collection at the front of the cell, and a 470-nm laser was used as a semiconductor excitation light source from the back of the cell. The cell was connected to a peristaltic pump to keep the electrolyte fresh during the test. The working electrode was connected via a conductive copper foil, and the electrode was kept perpendicular to the laser.

Photoelectrochemical in situ ATR-FTIR tests

Photoelectrochemical in situ ATR-FTIR OTTO measurements were recorded on an FTIR (Bruker, INVENIO S) spectrometer. The spectrometer was equipped with a Linglu Instruments EC-IR-III cell, and the ATR was tested by single bounce zinc selenide crystals in internal reflection thin-layer OTTO mode. Simulated sunlight was used as a light source at the top of the cell, which is described in Supplementary Fig. 17.

Characterization of Ca^{2+} and Mg^{2+} ions using ion chromatography

Analysis of the concentrations of Ca^{2+} and Mg^{2+} ions contained in the electrolyte at the cathode side was carried out using an ion chromatograph (SHINE, CIC-D160). The tests were performed as an automatic injection (1-h intervals) for 22 h of testing.

Detection of H_2 and O_2 via gas chromatography

The H_2 and O_2 production experiments were conducted in a sealed quartz electrolysis cell (37 ml) using a typical three-electrode system in seawater at pH 10 and at 1.2 V_{RHE}. The system was purged with argon gas (0.2 l min^{-1}) for 30 min before photoelectrochemical measurement. The gaseous products generated by PEC electrolysis in the anode chamber headspace (25 ml) were analysed each hour using a gas chromatograph (Shimadzu, GC-2014C) by taking 1 ml of electrolyte, with the process recorded over 22 h. The volume of the anode chamber headspace was calculated using the water displacement method. To obtain calibration curves for H_2 and O_2, gas chromatography was used to quantify various volumes of H_2 standard gas (0–0.1 ml) and O_2 standard gas (0–0.4 ml). The molar quantities of H_2 and O_2 standard gases were calculated on the basis of the ideal gas law, thereby obtaining calibration curves for H_2 and O_2 (linear relationship between peak area and the molar quantity of H_2 and O_2 standard gases). The FE of H_2 was calculated using equation (5):

$$\mathrm{FE}(\mathrm{H_2}) = \frac{n_{\mathrm{H_2}}(\mathrm{mol}) \times n \times F}{Q} \times 100\% \qquad (5)$$

where Q represents the total coulombs applied (C), n_{H_2} represents the amount of H_2 produced (mol), n represents the number of electrons transferred (2 for H_2) and F represents the Faraday constant (96.485 C mol^{-1}).

Reporting summary

Further information on research design is available in the Nature Portfolio Reporting Summary linked to this article.

Data availability

The data that support the findings of this study are available from the corresponding authors upon reasonable request. Source data are provided with this paper.

References

1. Chung, M. et al. Direct propylene epoxidation via water activation over Pd–Pt electrocatalysts. *Science* **383**, 49–55 (2024).
2. Fan, R. et al. Ultrastable electrocatalytic seawater splitting at ampere-level current density. *Nat. Sustain.* **7**, 158–167 (2024).
3. Choi, S. et al. A reflection on sustainable anode materials for electrochemical chloride oxidation. *Adv. Mater.* **35**, 2300429 (2023).
4. Zhao, S. et al. Selective electrosynthesis of chlorine disinfectants from seawater. *Nat. Sustain.* **7**, 148–157 (2024).
5. Yang, J. et al. CO_2-mediated organocatalytic chlorine evolution under industrial conditions. *Nature* **617**, 519–523 (2023).
6. Zeradjanin, A. R. The era of stable electrocatalysis. *Nat. Catal.* **6**, 458–459 (2023).
7. Janssen, L. J. J., Starmans, L. M. C., Visser, J. G. & Barendrecht, E. Mechanism of the chlorine evolution on a ruthenium oxide/titanium oxide electrode and on a ruthenium electrode. *Electrochim. Acta* **22**, 1093–1100 (1977).
8. Faita, G. & Fiori, G. Anodic discharge of chloride ions on oxide electrodes. *J. Appl. Electrochem.* **2**, 31–35 (1972).
9. Ha, H. et al. Highly selective active chlorine generation electrocatalyzed by Co_3O_4 nanoparticles: mechanistic investigation through in situ electrokinetic and spectroscopic analyses. *J. Phys. Chem. Lett.* **10**, 1226–1233 (2019).
10. Karlsson, R. K. B. & Cornel, A. Selectivity between oxygen and chlorine evolution in the chlor-alkali and chlorate processes. *Chem. Rev.* **116**, 2982–3028 (2016).
11. Exner, K. S. Design criteria for the competing chlorine and oxygen evolution reactions: avoid the OCl adsorbate to enhance chlorine selectivity. *Phys. Chem. Chem. Phys.* **22**, 22451–22458 (2020).
12. Vos, J. G., Venugopal, A., Smith, W. A. & Koper, M. T. M. Competition and selectivity during parallel evolution of bromine, chlorine and oxygen on IrO_x electrodes. *J. Catal.* **389**, 99–110 (2020).
13. Lim, T. et al. Atomically dispersed Pt–N_4 sites as efficient and selective electrocatalysts for the chlorine evolution reaction. *Nat. Commun.* **11**, 412 (2020).
14. Liu, H. et al. High-performance alkaline seawater electrolysis with anomalous chloride promoted oxygen evolution reaction. *Angew. Chem. Int. Ed.* **62**, e202311674 (2023).
15. Yao, Y. et al. Single atom Ru monolithic electrode for efficient chlorine evolution and nitrate reduction. *Angew. Chem. Int. Ed.* **61**, e202208215 (2022).
16. Moreno-Hernandez, I. A., Brunschwig, B. S. & Lewis, N. S. Crystalline nickel, cobalt, and manganese antimonates as electrocatalysts for the chlorine evolution reaction. *Energy Environ. Sci.* **12**, 1241–1248 (2019).

17. Liu, J. et al. Rationally designing efficient electrocatalysts for direct seawater splitting: challenges, achievements, and promises. *Angew. Chem. Int. Ed.* **61**, e202210753 (2022).
18. Tong, W. et al. Electrolysis of low-grade and saline surface water. *Nat. Energy* **5**, 367–377 (2020).
19. Miao, J. et al. Supramolecular catalyst with [$FeCl_4$] unit boosting photoelectrochemical seawater splitting via water nucleophilic attack pathway. *Nat. Commun.* **15**, 2023 (2024).
20. Zhao, Y. et al. A hydrogen farm strategy for scalable solar hydrogen production with particulate photocatalysts. *Angew. Chem. Int. Ed.* **59**, 9653–9658 (2020).
21. Qi, Y. et al. Efficient overall water splitting of a suspended photocatalyst boosted by metal-support interaction. *Joule* **8**, 193–203 (2024).
22. Kuang, Y. et al. Ultrastable low-bias water splitting photoanodes via photocorrosion inhibition and in situ catalyst regeneration. *Nat. Energy* **2**, 16191 (2016).
23. Ye, S. et al. Mimicking the key functions of photosystem II in artificial photosynthesis for photoelectrocatalytic water splitting. *J. Am. Chem. Soc.* **140**, 3250–3256 (2018).
24. Rahaman, M. et al. Solar-driven liquid multi-carbon fuel production using a standalone perovskite–$BiVO_4$ artificial leaf. *Nat. Energy* **8**, 629–638 (2023).
25. Qi, Y. et al. Unraveling of cocatalysts photodeposited selectively on facets of $BiVO_4$ to boost solar water splitting. *Nat. Commun.* **13**, 484 (2022).
26. Kim, T. W. & Choi, K.-S. Nanoporous $BiVO_4$ photoanodes with dual-layer oxygen evolution catalysts for solar water splitting. *Science* **343**, 990–994 (2014).
27. Lee, D. K. & Choi, K.-S. Enhancing long-term photostability of $BiVO_4$ photoanodes for solar water splitting by tuning electrolyte composition. *Nat. Energy* **3**, 53–60 (2018).
28. Gao, R.-T. et al. Dynamic semiconductor–electrolyte interface for sustainable solar water splitting over 600 hours under neutral conditions. *Sci. Adv.* **9**, eade4589 (2023).
29. Haverkamp, R. G., Kappen, P., Sizeland, K. H. & Wallwork, K. S. Niobium K-edge X-ray absorption spectroscopy of doped TiO_2 produced from ilmenite digested in hydrochloric acid. *ACS Omega* **7**, 28258–28264 (2022).
30. Kumar, A. et al. Probing the electronic and local structure of $Sr_{2-x}La_xCoNbO_6$ using near-edge and extended x-ray absorption fine structures. *Phys. Rev. B* **105**, 245155 (2022).
31. Markina, D. I. et al. Perovskite nanowire laser for hydrogen chloride gas sensing. *ACS Nano* **17**, 1570–1582 (2023).
32. Liang, J. et al. Electroreduction of alkaline/natural seawater: self-cleaning Pt/carbon cathode and on-site co-synthesis of H_2 and Mg hydroxide nanoflakes. *Chem* **10**, 3067–3087 (2024).
33. Pardo-Jaramillo, S., Munoz-Villamizar, A. & Gomez-Gonzalez, J. E. Unveiling the influence of COVID-19 on the online retail market: a comprehensive exploration. *J. Retail. Consum. Serv.* **75**, 103538 (2023).
34. Zhu, W. et al. Energy-efficient electrosynthesis of high value-added active chlorine coupled with H_2 generation from direct seawater electrolysis through decoupling electrolytes. *Angew. Chem. Int. Ed.* **63**, e202319798 (2024).
35. Mukherjee, I., Ghosh, A., Bhadury, P. & De, P. Matrix assisted antibacterial activity of polymer conjugates with pendant antibiotics, and bioactive and biopassive moieties. *J. Mater. Chem. B* **7**, 3007–3018 (2019).
36. Behler, J. & Parrinello, M. Generalized neural-network representation of high-dimensional potential-energy surfaces. *Phys. Rev. Lett.* **98**, 146401 (2007).
37. Nørskov, J. K. et al. Origin of the overpotential for oxygen reduction at a fuel-cell cathode. *J. Phys. Chem. B* **108**, 17886–17892 (2004).
38. Yu, J. & Kudo, A. Effects of structural variation on the photocatalytic performance of hydrothermally synthesized $BiVO_4$. *Adv. Funct. Mater.* **16**, 2163–2169 (2006).
39. Guo, J. et al. Direct seawater electrolysis by adjusting the local reaction environment of a catalyst. *Nat. Energy* **8**, 264–272 (2023).
40. Hao, Y. et al. Switching the oxygen evolution mechanism on atomically dispersed Ru for enhanced acidic reaction kinetics. *J. Am. Chem. Soc.* **145**, 23659–23669 (2023).

Acknowledgements

The work was supported by the National Science and Technology Major Project (grant no. 2022YFA1205200), the National Natural Science Foundation of China (grant nos 22269016, 22479083 and 22405138) and the Group Project of Developing Inner Mongolia through Talents from the Talents Work Leading Group under the CPC Inner Mongolia Autonomous Regional Committee (grant no. 2025TYL03). N.T.N. acknowledges NSERC, FRQNT and QCAM for financial support. We thank Y. Li at the University of Electronic Science and Technology of China for the discussion of this work.

Author contributions

L. Wu, R.-T.G. and L. Wang conceived the idea, designed the experiments and supervised the research project. R.-T.G. and Z.G. conducted the experiments and characterizations under discussion with N.T.N., X.L. and L. Wang. R.-T.G. analysed the data and wrote the paper. J.C. performed the modelling and simulation. L. Wu and L. Wang revised the paper. All the authors contributed to the experiments and discussion of the paper.

Competing interests

The authors declare no competing interests.

Additional information

Supplementary information The online version contains supplementary material available at https://doi.org/10.1038/s41893-025-01530-y.

Correspondence and requests for materials should be addressed to Lei Wang or Limin Wu.

Peer review information *Nature Sustainability* thanks Hao Li and the other, anonymous, reviewer(s) for their contribution to the peer review of this work.

nature portfolio

Corresponding author(s): Lei Wang, Limin Wu

Last updated by author(s): Feb 20, 2025

Reporting Summary

Nature Portfolio wishes to improve the reproducibility of the work that we publish. This form provides structure for consistency and transparency in reporting. For further information on Nature Portfolio policies, see our Editorial Policies and the Editorial Policy Checklist.

Statistics

For all statistical analyses, confirm that the following items are present in the figure legend, table legend, main text, or Methods section.

n/a	Confirmed	
☐	☒	The exact sample size (*n*) for each experimental group/condition, given as a discrete number and unit of measurement
☐	☒	A statement on whether measurements were taken from distinct samples or whether the same sample was measured repeatedly
☐	☒	The statistical test(s) used AND whether they are one- or two-sided *Only common tests should be described solely by name; describe more complex techniques in the Methods section.*
☐	☒	A description of all covariates tested
☐	☒	A description of any assumptions or corrections, such as tests of normality and adjustment for multiple comparisons
☐	☒	A full description of the statistical parameters including central tendency (e.g. means) or other basic estimates (e.g. regression coefficient) AND variation (e.g. standard deviation) or associated estimates of uncertainty (e.g. confidence intervals)
☐	☒	For null hypothesis testing, the test statistic (e.g. *F*, *t*, *r*) with confidence intervals, effect sizes, degrees of freedom and *P* value noted *Give P values as exact values whenever suitable.*
☐	☒	For Bayesian analysis, information on the choice of priors and Markov chain Monte Carlo settings
☐	☒	For hierarchical and complex designs, identification of the appropriate level for tests and full reporting of outcomes
☐	☒	Estimates of effect sizes (e.g. Cohen's *d*, Pearson's *r*), indicating how they were calculated

Our web collection on statistics for biologists contains articles on many of the points above.

Software and code

Policy information about availability of computer code

Data collection	All the data collection/data analysis software/tools/algorithms/packages used in the study are clearly mentioned in the manuscript and are also listed here in the reporting summary.
Data analysis	All the data collection/data analysis software/tools/algorithms/packages used in the study are clearly mentioned in the manuscript.

For manuscripts utilizing custom algorithms or software that are central to the research but not yet described in published literature, software must be made available to editors and reviewers. We strongly encourage code deposition in a community repository (e.g. GitHub). See the Nature Portfolio guidelines for submitting code & software for further information.

Data

Policy information about availability of data

All manuscripts must include a data availability statement. This statement should provide the following information, where applicable:

- Accession codes, unique identifiers, or web links for publicly available datasets
- A description of any restrictions on data availability
- For clinical datasets or third party data, please ensure that the statement adheres to our policy

The data are available from the corresponding author upon resonable request. Source data are provided with this paper.

Research involving human participants, their data, or biological material

Policy information about studies with human participants or human data. See also policy information about sex, gender (identity/presentation), and sexual orientation and race, ethnicity and racism.

Reporting on sex and gender	None.
Reporting on race, ethnicity, or other socially relevant groupings	None.
Population characteristics	None.
Recruitment	None.
Ethics oversight	None.

Note that full information on the approval of the study protocol must also be provided in the manuscript.

Field-specific reporting

Please select the one below that is the best fit for your research. If you are not sure, read the appropriate sections before making your selection.

☐ Life sciences ☐ Behavioural & social sciences ☒ Ecological, evolutionary & environmental sciences

For a reference copy of the document with all sections, see nature.com/documents/nr-reporting-summary-flat.pdf

Ecological, evolutionary & environmental sciences study design

All studies must disclose on these points even when the disclosure is negative.

Study description	This work describes a 篇photoelectrochemical synthetic disinfectant from nature seawater without Cl2 as an intermediate.
Research sample	A chloride-mediated NbClOx/BiVO4 photoanode.
Sampling strategy	The photoanode sample size was 1 cm2 for PEC measurement.
Data collection	Rui-Ting Gao and Zehua Gao collected the data.
Timing and spatial scale	In the experiments for taking more than 1-1.5 years.
Data exclusions	No data was excluded.
Reproducibility	All the data were repeated more than three times.
Randomization	None.
Blinding	None.

Did the study involve field work? ☐ Yes ☒ No

Reporting for specific materials, systems and methods

We require information from authors about some types of materials, experimental systems and methods used in many studies. Here, indicate whether each material, system or method listed is relevant to your study. If you are not sure if a list item applies to your research, read the appropriate section before selecting a response.

Materials & experimental systems

n/a	Involved in the study
☒	☐ Antibodies
☒	☐ Eukaryotic cell lines
☒	☐ Palaeontology and archaeology
☒	☐ Animals and other organisms
☒	☐ Clinical data
☒	☐ Dual use research of concern
☒	☐ Plants

Methods

n/a	Involved in the study
☒	☐ ChIP-seq
☒	☐ Flow cytometry
☒	☐ MRI-based neuroimaging

Plants

Seed stocks	None.
Novel plant genotypes	None.
Authentication	None.